A&A 444, 187–200 (2005)
DOI: 10.1051/0004-6361:20042562

Astronomy & Astrophysics

Absorption and scattering by interstellar dust: an XMM-Newton observation of Cyg X-2

E. Costantini[1,2], M. J. Freyberg[3], and P. Predehl[3]

[1] SRON National Institute for Space Research, Sorbonnelaan, 2, 3584CA, Utrecht, The Netherlands
[2] Astronomical Institute, Utrecht University, PO Box 80000, 3508TA Utrecht, The Netherlands
[3] Max-Planck-Institut für extraterrestrische Physik, Giessenbachstr. 1, 85748 Garching bei München, Germany

Received 17 December 2004 / Accepted 28 July 2005

ABSTRACT

We present results of the XMM-*Newton* observation of the bright X-ray binary Cyg X-2. In our analysis we focus on the absorption and scattering of the X-ray emission by interstellar dust distributed along the line of sight. The scattering halo around Cyg X-2, observed with the CCD detector EPIC-pn, is well detected up to ~7 arcmin and contributes ~5–7% to the total source emission at 1 keV, depending on the dust size distribution model considered. For the first time spatially resolved spectroscopy of a scattering halo is performed. In the halo spectrum we clearly detect the signature of the interstellar dust elements: O, Mg, and Si. In the 0.4−2 keV band, the spectral modeling of the halo shows a major contribution of silicates (olivine and pyroxene). The spatial analysis of the halo surface brightness profile shows that the dust is smoothly distributed toward Cyg X-2 at least for ~60% of the path to the source. However, given the substantial pile-up, we could not investigate fainter or narrower components of the halo. Within this observation limit, the data do not show preference for a specific dust size distribution. In this analysis we used the Mie theory to compute the differential scattering cross section. The RGS data were used to investigate the ISM absorption. The absorption spectrum shows complexity around the oxygen edge at ~0.54 keV, which cannot be explained in a unique way: it involves either absorption by molecular oxygen or ionized atomic oxygen, as proposed in other studies of Cyg X-2. Combining the RGS results with the additional information on dust grains provided by the EPIC-pn spectrum of the scattered radiation we estimate a column density for dust absorption by oxygen, provided that it is locked in silicate grains.

Key words. ISM: dust, extinction – X-rays: ISM – scattering – stars: binaries: general

1. Introduction

The observed light from a source is obscured by the interstellar matter (ISM) through the combination of two processes: absorption and scattering. Absorption is due to both gas and dust, whereas scattering is attributed to dust alone. Differently from the IR to UV wavelengths range, in the X-ray regime the observation of absorption and scattering by interstellar dust (ID) are strongly coupled. Thus, in the X-ray regime, the two extinction mechanisms can be simultaneously observed and studied. If an X-ray emitter is located behind a layer of dust, its radiation will be absorbed and at the same time scattered into the direction of the observer. In the X-rays the scattering mechanism is no longer explained by the simple Rayleigh formula. In particular the scattering angle is in this case very small ($\theta_{\rm scatt} \propto (\lambda/a) \ll 1^\circ$), forward directed, dependent on the wavelength of the incident photon (λ) and the size (a) of the grain. The small scattering angle results in a halo of diffuse emission around the source (Overbeck 1965). The energy range in which absorption and scattering can be studied, is a strong function of the equivalent hydrogen column density of the medium ($N_{\rm H}$). Indeed the X-ray radiation is obscured by absorption depending on the value of $N_{\rm H}$: $I = I_0 {\rm e}^{-N_{\rm H}\sigma}$, where I_0 is the source radiation and σ is the absorption cross section. Through the analysis of the absorbed spectrum, information on the chemistry, column density and abundances of the ID grains can be inferred. Simultaneously, the spectral and spatial properties of the X-ray halos can be analyzed. The halo intensity, angular extension, and spectral distribution are a function of the size distribution and composition of the scatterers (the dust grains), their distribution along the line of sight, and the spectral properties of the source illuminating them.

Sources with faint halos have a hydrogen column density which is low enough to not completely absorb the soft X-rays. High sensitivity instruments are needed to study the emission of the scattering halo, which is very weak compared to the brightness of a background source (up to 20% of the soft emission, Predehl & Klose 1996). Faint halos are important to study ID chemistry. Indeed the energy range where scattering occurs (approximately 0.3−2 keV), includes possible features of ID components, primarily oxygen (0.54 keV), magnesium (1.3 keV), and silicon (1.84 keV) (Predehl & Klose 1996; Draine 2003, hereinafter D03). An energy resolution of ~80−150 eV over the energy band of interest for the scattering

process, makes it possible to spectroscopically investigate the features of a faint halo. Previous studies of scattering halo profiles were carried out with *Einstein* (e.g. Mauche & Gorenstein 1986; Gallagher et al. 1995) and ROSAT (Smith & Dwek 1998; Predehl & Schmitt 1995, hereinafter PS95). According to those findings, the ID size distribution appeared to be consistent with the Mathis et al. (1977) (hereinafter MRN) model. The MRN model includes a mixture of carbonaceous and silicate materials, with size distribution $a^{-3.5}$, for $0.001 < a < 0.25$ μm. Alternative grain size distribution models have been proposed, differing mostly in the chosen boundaries of the grain size range, the slope of the distribution and the inner structure of the grain itself (Mathis & Whiffen 1989; Landgraf et al. 2000; Weingartner & Draine 2001, hereinafter WD01). From ROSAT data (Nova V1974 Cygni, Draine & Tan 2003) and the *Chandra* observation of GX 13+1 (Smith et al. 2002) the role of grains of size much larger than 0.4 μm has been stated not to play a major role, at least in the diffuse ISM, contrary to the Solar System environment, where grains up to 1 μm should have a significant contribution (Witt et al. 2001). On the other side of the range of the grain size, a better understanding of the infra-red spectrum of ID allowed to state the importance of ultra-small particles, the Aromatic Polycyclic Hydrocarbons (PAH), with radius $a < 30$ Å. Such a contribution was included in the WD01 model.

Finally, it has been recognized that a simple analytical computation of the differential scattering cross section, the so-called Rayleigh-Gans (RG) approximation, could be misleading if applied to halo energies <1 keV and/or large grains $a > 0.25$ μm. The full Mie theory (Mie 1908), from which the RG approximation is derived, had to be used (Smith & Dwek 1998; Draine & Tan 2003). The models applied to X-ray scattering halos are the result of a deeper knowledge of ID properties gathered at longer wavelengths. Due to the low resolution of early X-ray instruments, only integral properties of the dust could be studied, adding relatively little information on the nature of ID. On the contrary, with the X-ray observatories now flying, we can address other issues like: *(i)* the chemical properties of dust particles that scatter X-rays, *(ii)* abundances and depletion in the ISM, and *(iii)* the actual distribution of dust along the line of sight.

In this paper we present the RGS and EPIC-pn analysis of Cyg X-2, located at Galactic coordinates $l = 87.33°$, $b = -11.32°$, behind a dust layer with equivalent $N_{\rm H}$ column density of the order of $\sim 2 \times 10^{21}$ cm^{-2}, which produces a relatively weak scattering halo. This makes Cyg X-2 an ideal candidate to study both the spatial and spectral distribution of the halo at energies softer than 2 keV. The fractional halo intensity of Cyg X-2, defined as the intensity of the halo extended emission over the total observed emission, was estimated from ROSAT-PSPC to be 3.9% at 1.06 keV (PS95). Now, with the high sensitivity of XMM-*Newton*, the halo can be resolved and analyzed down to 0.4 keV with the EPIC-pn. Absorption by the ISM toward the line of sight of Cyg X-2 was studied with the RGS. Recently Cyg X-2 was studied by Takei et al. (2003), using *Chandra*-LETG and by Juett et al. (2004) using *Chandra*-HETG. In each analysis, the absorption features in the spectral region of the oxygen edge were interpreted in different ways. Takei et al. (2003) claimed to have detected absorption by molecular oxygen, while Juett et al. (2004) interpret those features in terms of mildly ionized oxygen in the ISM.

The paper is organized as follows: In Sect. 2 the principles of the scattering halo theory are presented. In Sect. 3 the analysis of RGS and EPIC-pn data of Cyg X-2 is shown. Section 4 describes the careful extraction of the information on scattered radiation. Section 5 is then devoted to the spatial and the spectral modeling of the scattered halo. Finally, in Sect. 6 we discuss our results, and in Sect. 7 the conclusions of this work are shown.

2. The halo theory

The intensity of the light scattered by dust at a scattering angle $\theta_{\rm sca}$, assuming spherical grains and single scattering has the following general form (e.g., Mathis & Lee 1991):

$$I(\theta_{\rm sca}) = \int_{E_{\rm min}}^{E_{\rm max}} F(E){\rm d}E \int_{a_{\rm min}}^{a_{\rm max}} n(a){\rm d}a \times \int_0^1 \frac{\tilde{f}(x)}{(1-x)^2} \frac{{\rm d}\sigma}{{\rm d}\Omega}{\rm d}x. \quad (1)$$

$F(E)$ is the spectral energy distribution of the source; a is the grain radius with number density $n(a)$; x is the fractional distance of the total path, from the source ($x = 1$) to the observer ($x = 0$), at which the scattering occurs; and $\tilde{f}(x)$ is the normalized spatial distribution of the scattering sites. Since we consider dust that is evenly distributed, $\tilde{f}(x) = 1$. For the scattering angle $\theta_{\rm sca}$, it holds that $\theta_{\rm sca} = \theta_{\rm obs}/(1-x)$. The term ${\rm d}\sigma/{\rm d}\Omega$ is the differential scattering cross section, a function of θ, a and E. There are two critical terms in Eq. (1). One is $n(a)$, which depends on the physical and chemical state of the dust grains. The other crucial term in evaluating the scattered emission is the differential scattering cross section for which the exact solution is given by the Mie theory (Mie 1908; van de Hulst 1957). This describes the scattering and absorption of an electromagnetic wave by spherical solid particles.

Quantitatively, the refraction index m of a given material can be written as (e.g., Henke et al. 1993):

$$m = 1 - \frac{r_{\rm e}\lambda^2}{2\pi} \sum_q n_q f_q(0) \quad (2)$$

where $r_{\rm e}$ is the classical electron radius, n_q the number density of the atom q. The quantity $f_q(0)$ is the complex forward atomic scattering factor for the element q. This definition only holds for small scattering angles, as is the case in the X-ray band, or for wavelengths that are large compared to the electron density of the scattering medium. For each element, the imaginary and real part of $f = f' + {\rm i}f''$ are related to each other through the Kramers-Kronig relations (e.g. Henke et al. 1993; D03):

$$f'(\omega) = \frac{2}{\pi} \int_0^\infty \frac{f''(\omega')\omega'{\rm d}\omega'}{\omega^2 - \omega'^2} \quad (3)$$

$$f''(\omega) = \frac{\omega\mu(\omega)}{2\pi n_q r_{\rm e} c}, \quad (4)$$

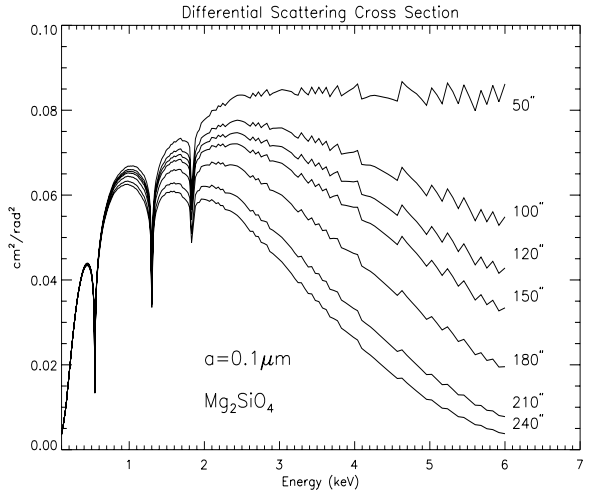

Fig. 1. The scattering cross section, calculated using the Mie theory, at specific scattering angles vs. energy for Mg_2SiO_4. A single grain size of 0.1 μm is considered.

where $\mu(\omega)$ is the absorption coefficient at the incident energy $E = \hbar\omega$. Here the assumption is that for a given compound the dielectric function is the sum of the single atom contributions. However, at the threshold energy, the absorption coefficient strongly depends on the chemical compound. The interaction between a photoelectron wave and all the other waves backscattered by the neighboring atoms creates modulations in the absorption cross section. These are in general called X-ray Absorption Fine Structure (XAFS). The XAFS features, which are few tenth of angstroms wide, have been recently recognized in high energy resolution absorption spectra of some astronomical sources (e.g., Lee et al. 2002). Only instruments with energy resolution better than $\Delta\lambda \sim 0.02$ Å can resolve these features. The differential scattering cross section, calculated using the Mie approach, as a function of energy is displayed in Fig. 1 for various scattering angles, considering the case of Mg_2SiO_4 and a grain size of 0.1 μm. The presence of $\mu(\omega)$ in the scattering cross section causes spikes at the K-edge of a given element, as seen in the figure. We note also that at the softer energies we do not expect a dramatic change in the spectral shape of the differential cross section as a function of the scattering angle.

In our observation, the Cyg X-2 halo is visible down to 0.4 keV, as the hydrogen column density toward the source is relatively low ($N_{\rm H} \sim 2.17 \times 10^{21}$ cm^{-2}, as measured from the HI emission, Dickey & Lockman 1990). Therefore we need to evaluate the $\frac{d\sigma}{d\Omega}$ term in Eq. (1) with the Mie theory. We then compare the predicted scattered intensity (Eq. (1)), calculated using the classical MNR model and the WD01 model for $n(a)$, with our data.

3. Data analysis

Cyg X-2 was observed by XMM-*Newton* EPIC-pn (Strüder et al. 2001) in full-frame mode, EPIC-MOS (Turner et al. 2001) cameras, and the RGS high resolution spectrometers (den Herder et al. 2001) on June 3rd 2002 for 18.6 ks. The central CCDs of MOS1 and MOS2 were operated in timing mode and thus contain no imaging information. We therefore show data of EPIC-pn and RGS only.

We processed the data using the XMM-Newton Science Analysis Software (XMMSAS-5.4.1) as well as ad hoc routines not included in the standard software.

3.1. Cyg X-2 EPIC-pn spectral analysis

A single photon can lead to charges in a single pixel (referred to as *single events*), two neighboring pixels (*double events*), or three or four pixels (if the photon hits a region close to the corner of a pixel). Pile-up can occur when two photons hit the same pixel in the same read-out cycle (energy pile-up) or hit a neighboring pixel (pattern pile-up), leading to distortions in the pattern distribution of single and double events. The central pixels of the source image of Cyg X-2 are heavily piled up. A diagnostic tool (XMMSAS task `epatplot`) applicable to XMM-*Newton* EPIC CCDs makes use of the event pattern distributions, which can be precisely modeled as a function of energy for X-rays passing through the telescope in the absence of pile-up. From a comparison of such a modeled distribution with a *real* pattern distribution, the percentage of pile-up in a spectrum extracted from a given region can be estimated.

Out-of-Time (OOT) events occur during the read-out of a pn-CCD along the read-out direction. As these events are accumulated only within a short time and are distributed over the whole CCD length pile-up effects are a factor of 1000 smaller. After checking with the `epatplot` procedure, we used these events to model the broad band spectrum (0.4–10 keV) of the central source. In principle the absolute flux can be evaluated from the OOT events. In the case of extreme pile up this is no longer possible, due to the "pseudo-MIP" effect: If the charge within one pn-CCD pixel exceeds a threshold of about 15 keV this event is regarded as being due to a minimum ionizing particle (MIP) and all events in this CCD column and the neighboring columns for this read-out frame are rejected on board (pseudo-MIPs, Freyberg 2003). However, in the case of very strong pile-up this threshold can be triggered by normal X-rays. In extreme cases, in almost all frames the columns at the center of the PSF are rejected. These spatial exposure variations are not fully reflected in the event data files and in the XMMSAS software. The "pseudo-MIPs" have no appreciable influence on the source spectral shape; however, these rejected columns affect the determination of the flux measured from the OOT events. Indeed, the pseudo-MIP rejection occurs preferentially in the columns corresponding to the PSF core and therefore in the same columns as the bulk of the OOT events, which then get rejected. We modeled the spectrum extracted from the OOT events. Note that the source position, rather than the recorded position on the CCD, was used for the Charge Transfer Inefficiency (CTI) correction using XMMSAS. The soft EPIC-pn spectrum is well fitted with a multi-temperature black body for the accretion disk emission (Mitsuda et al. 1984) with $kT \sim 0.36$ keV at the inner radius, plus a comptonized black body spectrum for the emission of the neutron star (Titarchuk 1994). The soft (seed) photons have a temperature $kT_0 \sim 0.8$ keV before being Compton scattered

Table 1. Best fit parameters for the EPIC-pn spectrum of Cyg X-2 in the energy band 0.4–10 keV, with a disk black body at temperature $kT_{\rm db}$ (DISKBB in XSPEC, Mitsuda et al. 1984) and a comptonized spectrum (COMPTT in XSPEC, Titarchuk 1994), affected by extinction of gas and dust (TBABS in XSPEC, Wilms et al. 2000). See text for the definition of the parameters. Errors are given at 90% confidence level for one interesting parameter.

$N_{\rm H}$ ($\times 10^{22}$ cm^{-2})	0.19 ± 0.05
$kT_{\rm db}$ (keV)	0.36 ± 0.05
kT_0 (keV)	0.81 ± 0.03
kT (keV)	6.2 ± 0.1
τ	1.62 ± 0.07
$E_{\rm Fe}$ (keV)	6.67 ± 0.16
$\sigma_{\rm Fe}$ (keV)	$0.2^{+0.3}_{-0.1}$
$EW_{\rm Fe}$ (eV)	73 ± 53
χ^2/d.o.f.	1115/1111

to reach a temperature of $kT \sim 6.2$ keV in an electron cloud of thickness τ (Table 1). We found evidence of an emission line at energy $E \sim 6.7$ keV, consistent with fluorescent emission by ionized iron (e.g., Di Salvo et al. 2002). The soft spectrum is both absorbed by gas and dust and scattered by ID, i.e. light is deviated from our line of sight "subtracting" photons from the central source spectrum (PS95), We implemented in XSPEC a model for the scattering correction which is based on handy empirical relations: $\tau_{\rm sca} = 0.05 \times N_{\rm H} - 0.083$ and $A_{\rm V} = 0.56\, N_{\rm H} + 0.23$, where $\tau_{\rm sca}$ is the scattering optical depth and $N_{\rm H}$ is in units of 10^{21} cm^{-2}. This relation is based on the study of 25 ROSAT sources (PS95) and it is not critically model dependent as long as we are dealing with a relatively small correction for τ. The optical extinction $A_{\rm V}$ value is only 1.3 for Cyg X-2 (Bradt & McClintock 1983), therefore the influence of scattering in the spectrum is practically negligible in the fit for such a low intervening column density (PS95).

3.2. Cyg X-2 RGS spectral analysis

As the RGS covers only the 0.35–2 keV band, the hard component cannot be constrained, therefore the thermal comptonization parameters are fixed to the EPIC-pn best-fit values. The background spectrum contribution was evaluated using the "blank field" observations specific for RGS. This guarantees the omission of any halo contamination in the background. In the case of Cyg X-2, the halo contribution to the source spectrum is almost negligible, since the flux of the source is more than 20 times larger than the flux of the diffuse halo. We extracted the first and second order from RGS1 and RGS2 for a total of four data sets. The data below 7 Å are affected by low and poorly calibrated sensitivity and are rejected.

Absorption by oxygen in the ISM could be studied in detail in the spectral region around 0.54 keV. Takei et al. (2003) found a complex structure for the oxygen edge region in a *Chandra*-LETG observation of Cyg X-2. In their analysis they interpreted the spectrum in terms of absorption lines and edges from oxygen in both atomic and molecular form. Although the RGS energy resolution is approximately 44% less than LETG, we find similar complexity in the oxygen region: in particular a single oxygen edge at energy 0.543 keV is an unsatisfactory fit to the data. We first considered the approach of Takei et al. (2003) (*model 1* in Table 2). We included an additional edge in the fit, which improves the fit by $\Delta\chi^2/\Delta\nu = 39/1$ (corresponding to a significance higher than 99.5%). The two edge energies are fixed: 0.536 (23.13) and 0.543 (22.83) keV (Å), corresponding to compound and atomic oxygen, respectively. On the other hand, a third edge, strongly required by LETG data at 0.549 keV (22.58 Å, atomic oxygen), improves our fit only by $\Delta\chi^2/\Delta\nu = 5/1$ (significance 97.5%). At an energy of 0.524 ± 0.003 keV, consistent with the atomic oxygen 1s − 2p transition, an absorption line of equivalent width (EW) $1.45^{+0.22}_{-0.14}$ eV is clearly detected. Finally, at 0.530 ± 0.003 keV some absorption line-like residuals, in addition to the known instrumental absorption line (de Vries et al. 2003), still remain. Including at this position a second absorption line in the fit yields an energy that is interpreted as the 1s − 2p transition of compound oxygen (Fig. 2, upper panel). The measured EW is 1.41 ± 0.26 eV, consistent with the findings of Takei et al. (2003).

However, large uncertainties still remain in the laboratory measurements of oxygen bound with other elements and the identification of such features is not conclusive. Other laboratory measurements (e.g., McLaughlin & Kirby 1998; Gorczyca & McLaughlin 2000) of atomic oxygen around the K edge region would interpret the absorption structures as absorption

Table 2. RGS fitting results for the oxygen region in Cyg X-2. The parameters for the continuum emission are taken from the broad-band spectrum. The energies are measured in keV and the Equivalent Width (EW) in eV. Model 1 fits the O vicinity with 3 edges (two of which are from atomic O) and 2 absorption lines (one from atomic neutral O and the other from molecular O). Model 2 interprets the spectrum in terms of absorption by atomic O, either neutral or mildly ionized. Errors are given at 90% confidence for one interesting parameter.

	model 1	model 2
Lines		
E_1	0.524 ± 0.003	0.524 ± 0.003
EW_1	$1.45^{+0.22}_{-0.14}$	1.49 ± 0.17
E_2	0.530 ± 0.001	0.530 ± 0.001
EW_2	1.41 ± 0.26	1.44 ± 0.28
E_3	···	0.538 ± 0.001
EW_3	···	$0.44^{+0.19}_{-0.24}$
E_4	···	0.541 ± 0.001
EW_4	···	$1.01^{+0.15}_{-0.26}$
Edges		
E_1	0.536 fix.	···
τ_1	0.27 ± 0.06	···
E_2	0.543 fix.	0.543 ± 0.001
τ_2	0.45 ± 0.02	0.81 ± 0.02
E_3	0.549 fix.	···
τ_3	$0.09^{+0.07}_{-0.08}$	···

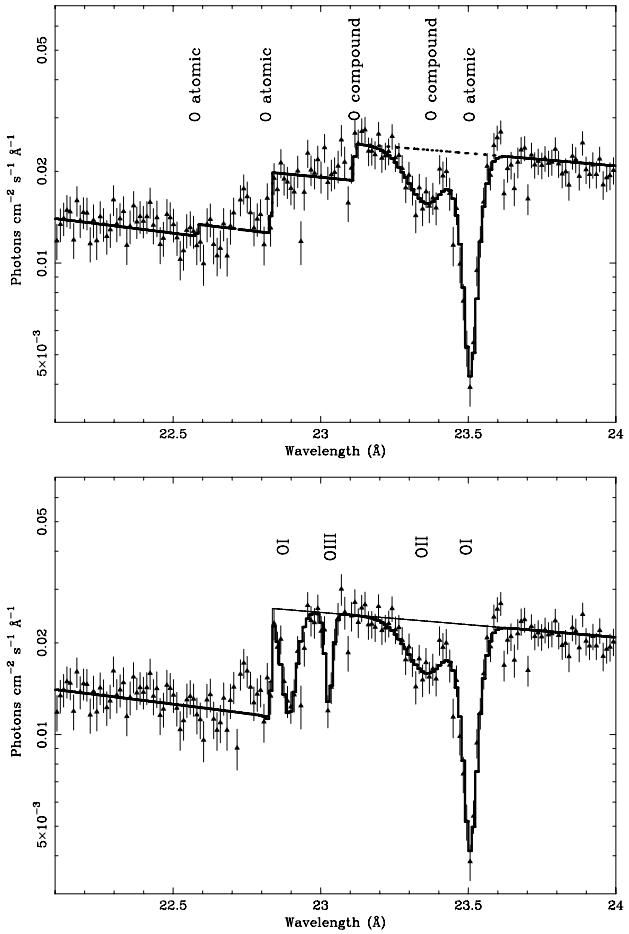

Fig. 2. Comparison between model 1 (*top*), and model 2 (*bottom*) used to fit the oxygen region, using the RGS data. Model 1 includes three absorption edges and two absorption lines. Model 2 includes one absorption edge and four absorption lines.

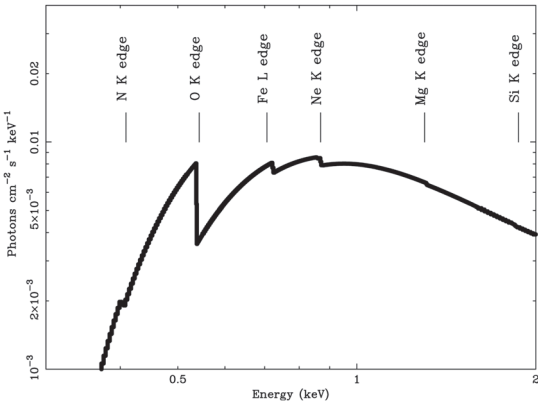

Fig. 3. ISM absorption edges predicted for $N_{\rm H} \sim 2.2\times10^{21}$ cm^{-2} using the best EPIC-pn best fit model, evaluated from the OOT events data. Mg (1.3 keV) and Si (1.84 keV) are only marginally evident in the model.

Table 3. Relevant absorption edges in the RGS spectrum of Cyg X-2. The energy, the corresponding wavelength, and the optical depth (τ) were obtained from the data. The equivalent total hydrogen column density $N_{\rm H}$ was derived from the ISM abundances of Wilms et al. (2000). These are to be compared with the best-fit $N_{\rm H}$ = (2.20 ± 0.02) × 10^{21} cm^{-2}, measured by RGS. Errors are given at 90% confidence level.

Element	Energy	Wavelength	τ	$N_{\rm H}$
	keV	Å		10^{21} cm^{-2}
N K-shell	0.409 (fixed)	30.31	0.15 ± 0.06	2.7 ± 1.1
O K-shell	0.543 (fixed)	22.83	0.81±0.10	2.8 ± 0.8
Fe L-shell	0.706 ± 0.01	17.56 ± 0.02	0.13 ± 0.01	2.8 ± 0.2
Ne K-shell	$0.869^{+0.02}_{-0.06}$	$14.26^{+0.10}_{-0.03}$	0.06 ± 0.03	1.8 ± 0.9

lines from neutral and ionized oxygen. This is called *model 2* in Table 2. The only two features in common with the Takei et al. interpretation are: the absorption edge at 0.543 keV (22.83 Å) and the 1s − 2p transition line at 0.524 ± 0.003 keV. The region between these two "standard" features is fit by an absorption line at 22.89 Å, consistent with the 1s − 3p transition of neutral atomic oxygen, and with another absorption line which would be consistent with a blend of unresolved lines of OIII (at 23.05 Å). Finally, the evident absorption line at 23.35 Å, also found by Takei et al., is interpreted as ionized atomic oxygen (OII), as predicted by Gorczyca & McLaughlin (2000) measurements (Fig. 2, lower panel). This interpretation (*model 2*) was also applied to *Chandra*-HETG data of a sample of bright galactic sources (Juett et al. 2004). Such an ionized component would be interpreted as ionization of the ISM, localized in the vicinity of the source. In Table 2 the results of the two models are shown; there is no significant difference in terms of goodness of fit.

The total equivalent hydrogen column density $N_{\rm H}$ = (2.20± 0.02) × 10^{21} cm^{-2}, as measured by the RGS, predicts K-shell absorption edges of nitrogen, oxygen, neon, and also iron L-shell, as shown in Fig. 3. The statistics of the present data allow the determination of the physical parameters of the absorption.

For each element j, we calculated the column density $N_j = \tau_j/\sigma_j$ using the photoelectric cross section computed from tabulated values (Henke et al. 1993; Verner & Yakovlev 1995). The optical depth τ_j was measured from an absorption edge model. The edge model was applied to our best fit continuum, but fixing to zero the abundance of the element j in the absorption model. Using the ISM abundances listed by Wilms et al. (2000), we derived the equivalent hydrogen column density. In general we find an agreement within the errors between the column densities so derived and the $N_{\rm H}$ found in our best-fit model (Table 3). We note that iron shows an overabundance of ∼20% compared to the Wilms et al. (2000) ISM value.

4. The analysis of the scattering halo

Thanks to the large effective area of the XMM-*Newton* telescopes, coupled with the large field of view and spectral resolution of EPIC-pn, the "pure" scattered radiation can be extracted from the halo spectrum. Thus for the first time we were able to

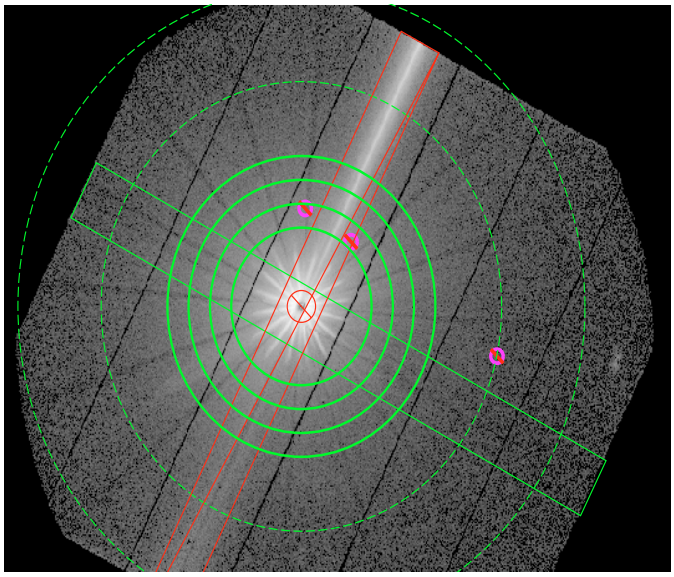

Fig. 4. EPIC-pn image of Cyg X-2 in the 0.5–3 keV band. The solid line annuli show three of the extraction regions specific for the halo spectral analysis (Fig. 7). The circles are drawn at 3.3, 4.3, 5.3, 6.3 arcmin. The dashed line annulus is the background. These regions were cut by the green rectangle across the detector (see Sect. 4.2). For the halo spatial analysis (Sect. 4.1) the annuli were instead logarithmically spaced. The barred regions were excluded from the data analysis: pile-up region (circle in the center), OOT events (box), and the serendipitous sources (points).

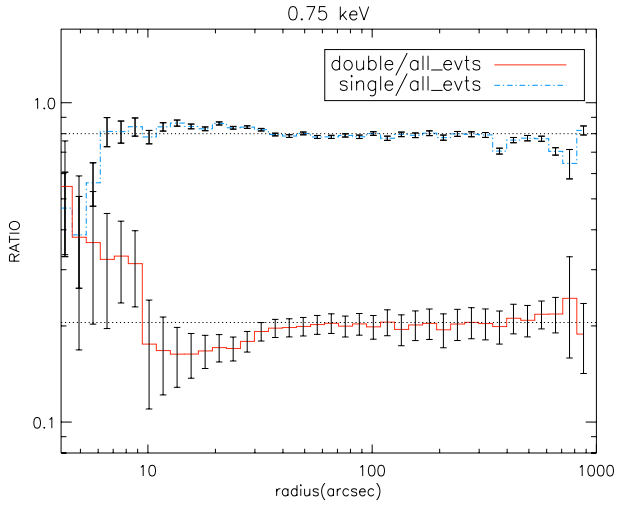

Fig. 5. Ratio between single events and all events (upper dash-dotted curve) and ratio between double and all events (lower solid curve), for EPIC-pn, around 0.75 keV. The dotted lines represent the values expected in absence of pile-up.

analyze both the spatial and the spectral distribution of the scattering halo. The diffuse emission brightness is a few percent of the central source flux. The subtraction of the Cyg X-2 contribution relies on *(i)* an accurate understanding of the instrumental scattering by the surface of the gold mirrors of the telescope and *(ii)* a careful handling of the pile-up, affecting the central part of the source. Pile-up distorts both the spectral shape and the surface brightness profile (SBP).

4.1. Halo spatial analysis

As a preliminary step, all spurious sources were removed from the data set. The *Simbad*[1] search reports 60 objects in the field of view of Cyg X-2 of which only 3 are known X-ray sources. These were not detected in our observation, but nevertheless the data at those positions were discarded (see Fig. 4). The SBP of the scattering halo was evaluated extracting the photons at selected energies between 0.4 and 2 keV in bins of 0.25 keV from logarithmically spaced annuli centered on the source, excluding the emission coming from the read-out streak due to OOT events. For the background we took an annulus from 9.5′ to 13′, avoiding the read-out streak region. The chosen background is consistent with the scaled value of the background taken from the "blank field" data for EPIC-pn (Read & Ponman 2003). For the extraction we took into account the different exposures of each quadrant of the detector selecting just the time intervals when all four quadrants were on at the same time. Any excluded region (serendipity sources, OOT events, regions outside the chip boundaries) was of course taken into account in the computation of the extraction area.

Pile-up is close to 100% at the center of the source. This causes the characteristic "hole" in the spatial profile, but to a lesser degree also distorts the profile shape up to many arcsecs from the source. In order to evaluate the dependence of pile-up as a function of the distance from the source, we extracted the radial profile of the source at different energies for single events, double events and the total events, selecting different *pattern* from the data. Where the count rate is low (i.e. no pile-up) the ratio of the radial profiles extracted with these different *patterns* (single, double and all events), should be a constant value (Fig. 5). We see that for single events pile-up affects the profile up to ∼40″; thus we studied the data only outside this radius. We divided the photon histogram by the exposure map, and the areas of the annuli, that was also corrected for the zones excluded in the photon extraction. Moreover, each photon is vignetting corrected by the ratio of the effective area at the aim point of the telescope and at the position where the photon itself is detected. The resulting radial intensity distribution is now in units of cts/s/arcsec^2. The next step is the subtraction of the PSF from the data. The model for the XMM-*Newton* PSF as a function of energy and off-axis angle was derived by the analysis of 110 point-like sources (Ghizzardi 2002). The instrumental PSF is described by a King profile:

$$PSF \propto \left(\frac{1}{[1+(r/r_c)^2]^{\alpha}}\right), \quad (5)$$

where r_c is the radius of the PSF core, and α the slope of the profile. The energy dependence[2] for these parameters is $\alpha = 1.525 - 0.015 \times E$ and $r_c = 6.636 - 0.305 \times E$. For a full description of the PSF modeling see Ghizzardi (2002). For each energy we considered in the halo spatial analysis, we used the appropriate King profile. We compared this PSF profile with

[1] http://simbad.u-strasbg.fr

[2] The off-axis dependence of the PSF is neglected as the sources we study are located on-axis.

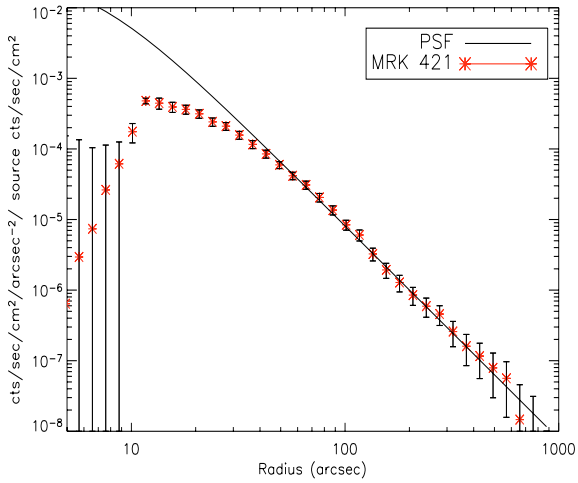

Fig. 6. Comparison between the PSF-model (solid line), Mrk 421 (asterisks) between 0.9 and 1 keV. For radii smaller than ∼30″, the flatness of the profile is mainly due to the mask used in the observation. The counts in this region are non zero due to a slight misalignment of the mask with respect to the source coordinates in this particular observation.

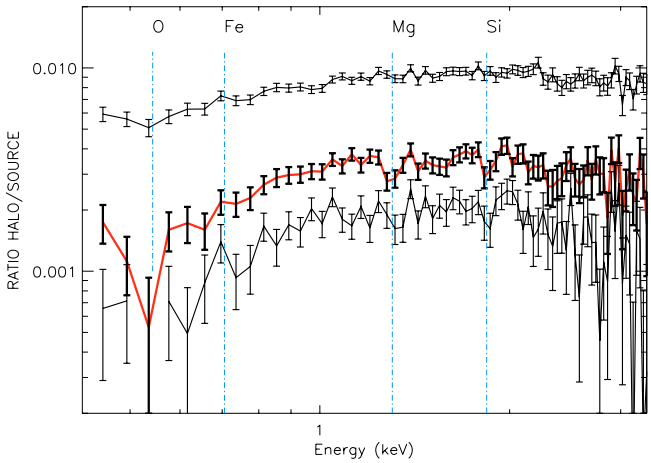

Fig. 7. The ratio between the halo spectra and the central source spectrum. At this stage the data are still convolved with the PSF. The spectra were extracted from annuli – *from top to bottom* – centered at 3.8, 4.8, and 5.8 arcmin respectively (Fig. 4). At larger radii the PSF contribution becomes less important. Dashed vertical lines: energies of relevant ID elements (O, Fe, Mg, Si). Error bars are 68% confidence level (1σ). The vertical axis units are arbitrary as the absolute flux of the source could not be recovered from the OOT events (Sect. 3.1).

the calibration target Mrk 421 (Fig. 6), which will be extensively used in this paper as a halo-free source, in comparison with Cyg X-2. This bright point-like source was observed in a special "masked" mode. In this submode the central 11×11 pixels (of size 4.128 arcsec each, i.e. a square of ∼45 arcsec or a half diagonal of ∼0.53 arcmin) were set as bad pixels and thus masked on board. This prevents the creation of pseudo-MIPs (Sect. 3.1) and thus the OOT events can be used to recover the source flux value as well as the spectral shape. Thus the Mrk 421 profile, also in units of cts/s/arcsec^2, could be easily normalized to the raw count rate (cts/s) of the source in a given energy bin.

Such a normalization was not straightforward for the Cyg X-2 profile, since the central pixels of the source image are unusable due to the strong pile up. However, since the absolute level of the Mrk 421 surface brightness profile (in units of arcsec^{-1}) is known, we could safely normalize the Cyg X-2 halo radial profile. We made the two profiles overlap in the interval between ∼40″−100″, where Cyg X-2 does not show significant scattered extended emission and therefore the profile is dominated by the instrumental PSF. We have seen above that the PSF profile slowly changes with energy, hence overlapping the source profile with the PSF considering a too large energy band would introduce additional uncertainty. For the largest energy bin we considered (0.25 keV, Sect. 5.1), the net uncertainty on the slope α is ±2%. As the halo analysis is confined to radii >40″, the uncertainty introduced by $r_c(E)$ is negligible. We note that in principle, to evaluate the spectral flux we could use either the OOT events or the RGS high resolution spectrum. The uncertainties in the cross calibration between PN and RGS flux may reach 20% and make the RGS data inappropriate for this purpose. The OOT events were also unusable for the normalization due to the pseudo-MIP effect (Sect. 3.1).

At the end of the procedure just described, the resulting SBP of Cyg X-2, which is the summed contribution of an extended emission and the instrumental profile, could be subtracted by the PSF and then modeled (Sect. 5.1).

4.2. Halo spectral analysis

For the study of the spatial variation of the spectrum we first selected radial distances from the source from 1.3′ to 7.3′ divided in annuli of 1′. The background was extracted from the same region as for the halo spatial analysis. A spatial selection[3], was applied to ensure that the energy response stays constant across the detector. In order to have a model-independent estimate of how the halo spectra may change as a function of the distance from the source, we normalized the spectra in the rings (in units of raw detector counts) to the source spectrum estimated from the OOT events (Sect. 3.1). In this way, first, all the features belonging to the X-ray emitter itself cancel out and, second, assuming that absorption by ID is rather uniform within the few arcmin across the halo, also the absorption component is eliminated from the halo spectrum. The result of this procedure is shown in Fig. 7. The spectra of the Cyg X-2 halo are plotted to illustrate the behavior of the halo with increasing angular distance from the source, as the PSF contribution becomes less important. The extraction regions of these spectra are marked in Fig. 4. Here the inner radii range from 3.3′ to 5.3′, where the halo is more relevant. Note that at this stage, the instrumental mirror scattering spectral energy distribution is still to be subtracted. The vertical axis of Fig. 7 is in arbitrary units as the absolute normalization of the source spectrum cannot be recovered from the OOT events (see Sect. 3.1). Below 2 keV, a decline of the curve is evident and the presence of three

[3] the RAW CCD coordinate selection was: RAWY = 180−199. This RAWY range always contains the source if it is observed on-axis and is well calibrated, and allows us to avoid the uncertainties related to the RAWY dependence of the energy response.

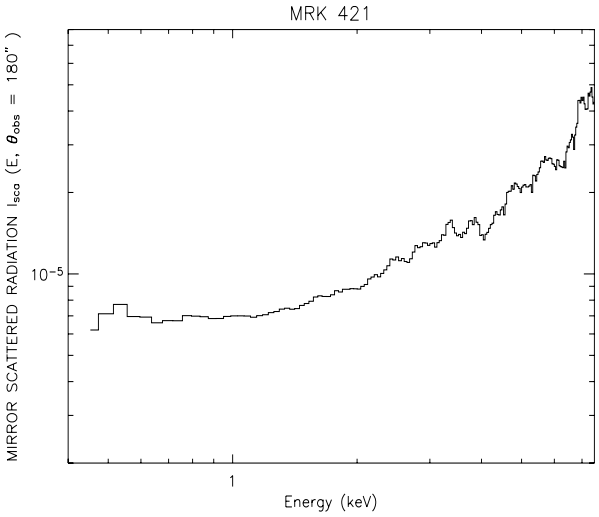

Fig. 8. XMM EPIC-pn pure-scattering mirror spectrum at a radius 180″ from the source, extracted from the halo-free source Mrk 421. We note a smooth increase of the scattering above 2 keV for larger radii.

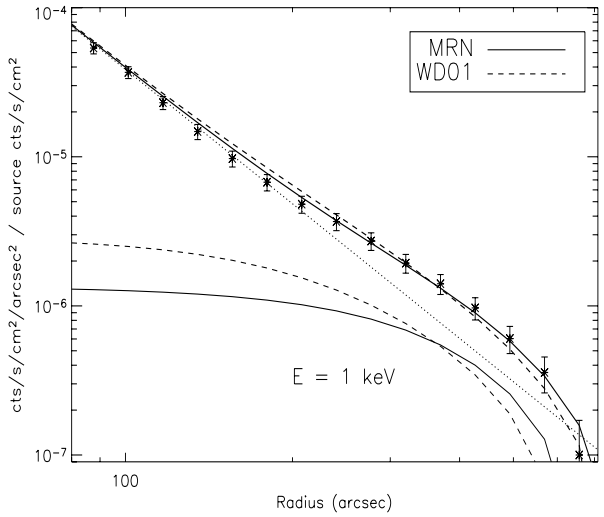

Fig. 9. The data (halo+PSF) (asterisks) compared to the PSF (dotted line) around 1 keV. The dashed and the solid thin lines are two different halo models (MRN and W01), while the solid and dashed thick lines indicate the best-fit to the total data (model+PSF) relative to MRN and WD01, respectively.

absorption features corresponding to the energy of O (0.54 keV), Mg (1.3 keV) and Si (1.84 keV) are observed. The vertical dashed lines indicate the position of these features and for completeness, the Fe L edge position (0.709 keV) is also marked. In the absence of any extended emission (i.e. for a point-like source) the result of the above exercise on the spectrum extraction is the pure instrumental mirror scattering. This was done for the point source Mrk 421, to which exactly the same procedure was applied (Fig. 8 for an example at radius 180″). Since the point-source data are real data (though with high statistics), they are still affected by noise. Thus, to avoid loss of information on the halo spectra, the Mrk 421 spectrum was smoothed before subtracting it from the data. The PSF spectrum does not change significantly as a function of the scattering angle at soft energies, keeping its almost constant shape between 0.4−1.2 keV. As we do not have precise information on the absolute flux of Cyg X-2, in order to perform the PSF subtraction we made the halo spectrum collected at each annulus coincide with the homologous spectrum of Mrk 421, in the spectral region where the emission is due to scattering by the telescope mirrors only (>3.5 keV). The PSF-subtracted scattered radiation is shown in Fig. 11 for an observed angle of 4.8′. From the lowest observed energy up to the silicon edge energy, the PSF subtraction is not a concern, as the extended emission is well above the PSF spectrum for a wide range of scattering angles (see Fig. 9 for an example at 1 keV). The comparison PSF-halo is less straightforward for the Si feature and the continuum just below 1.84 keV, as the scattered emission becomes weaker with respect to the PSF. In this region, a small difference in the chosen normalization may affect the results of the halo modeling. The PSF subtraction has the effect of making the Si feature appear even deeper than what already observed from the raw data (Fig. 7). If, for example, the normalization of the halo spectrum were ±10% of what we calculated, the error bars for the Si feature in the PSF-subtracted spectrum (Fig. 11) would increase of an additional 6%, considering that the ratio between the PSF and the raw data at this position is ∼30% at $\theta_{\rm obs} = 4.8'$.

5. The halo modeling

There are two critical terms in Eq. (1). One is the differential scattering cross section and the other is the assumed grain size distribution. For both the spatial and the spectral modeling of the scattering halo, we used the differential scattering cross section calculated using the Mie theory. For each value of the parameter $X = 2\pi\ a/\lambda$, where a is the grain size and λ is the wavelength of the incoming wave, we calculated the parameter $\mathrm{d}\sigma/\mathrm{d}\Omega$ for 115 scattering angles $\theta_{\rm sca}$ from 0 to 3°. The scattering cross section depends also on the diffraction index m which is determined by the material and is energy dependent. In this study we use the tabulated values of m for graphite, olivine, and pyroxene as determined by Henke et al. (1993) except in one case (Sect. 6.1), when we test the specific ID composition proposed in D03. In that case, the calculation for m takes into account the XAFS near the edges.

The code[4] (Wiscombe 1980) used to generate the scattering cross sections is reliable for $X < 2 \times 10^4$. For large values of a (say $a > 1.2\ \mu$m for $E = 2$ keV), the anomalous diffraction theory should be used (van de Hulst 1957). We ignore very large grains in our calculation since, as shown in Draine & Tan (2003), radii >0.4 μm contribute less than 1% at large scattering angles, and less than 20% at $\theta_{\rm sca} < 100''$. In bright sources, like Cyg X-2, pile-up hampers the possibility to investigate the halo at small scattering angles, where the effect of very large grains, or grains located very close to the source may be relevant (Predehl & Klose 1996). We also restricted our modeling to energies <2 keV, above which the halo contribution drops dramatically in the case of Cyg X-2.

[4] ftp://climate.gsfc.nasa.gov/pub/wiscombe/Single_Scatt/Homogen_Sphere/Exact_Mie/

Thus, the chosen grain size interval is 0.005–0.25 μm or 0.00035–0.8 μm when the MRN dust size distribution model or WD01 model is adopted, respectively. The dust size intervals were divided in 200 logarithmically spaced size bins. We allowed the power law index of the MRN distribution to vary by 20% around the typical value 3.5. WD01 tested their grain size distribution for two different values of the ratio of the total over selective optical extinction: $R_V = 3.1$ and 5.3, and for different carbon abundances. Cyg X-2 is located at galactic latitude $b = -11.3°$ where the ISM is diffuse (no CO detected, Dame et al. 2001), thus we considered $R_V = 3.1$. We used the set of parameters for slopes and coefficients of the dust distribution corresponding to a carbon abundance in PAH alone of 6×10^{-5} (Table 1 of Weingartner & Draine 2001). For both models, the lower and upper limit of the integral on the dust distribution parameter x were left as free parameters.

5.1. Spatial modeling of the halo

The SBP was extracted and subtracted from the PSF contribution as described in Sect. 4.1. At a fixed energy, the model has three free parameters (Eq. (1)): $d\sigma/d\Omega$, x, and $n(a)$. The best fit was reached through χ^2 minimization. We considered rays only scattered once before being observed. Double scattering occurs for optical depths τ_{sca} close to unity, indicating a very high dust column density (PS95, Costantini & Predehl 2005), which is not observed toward Cyg X-2. In Fig. 9, the Cyg X-2 SBP of the halo at 1 keV is shown. We tested the MRN and the WD01 for the dust size distribution. Both models provide an acceptable fit in terms of χ^2 ($\chi^2_{red} = 1.29$ and 1.33, respectively). The WD01 distribution spans a wider range of grain sizes. In particular, scattering by grains with size a in the range 0.25–0.4 μm have the effect of enhancing the halo at smaller radii ($\lesssim$200″). The intensity of the halo is parameterized by the scattering optical depth τ_{sca}, defined as: $I_{frac} = I_{halo}/I_{tot} = 1 - e^{-\tau_{sca}}$, where I_{halo} is the flux of the scattered emission, and I_{tot} is the total source emission (PS95). At 1 keV we measured $\tau_{sca} = 0.054 \pm 0.018$ and 0.067 ± 0.018 for the MRN or the WD01 model, respectively. The error quoted here is statistical and does not include any uncertainty in the background subtraction. The best fit shows a minimum and maximum value for the fractional path at which the scattering occurs, x, of ~0.001 and ~0.6, respectively. In this interval the halo profile shows a smooth distribution of dust along the line of sight up to a fractional distance $x \sim 0.6$, after which the halo is unaccessible due to pile-up. However, if the upper limit of x is constrained to be close to 1 (we fixed it at 0.99) indicating that we are actually observing scattering occurring at all distances, the fit worsens for both the WD01 and MRN models ($\Delta\chi^2 = 37$ for $\Delta\nu = 1$, corresponding to a significance >99.5%). We then extended this analysis to the energy range at which the halo is observable. In Fig. 10 we show the total scattering optical depth, derived from the SBP using energy intervals of 0.25 keV, in the energy range 0.4–1.9 keV. The large bin size smoothes out any features, leaving just the general shape the spectral energy distribution of the scattering optical depth. The solid line in Fig. 10 refers to the theoretical value of τ_{sca} as predicted by D03 at the mean energy of the extraction bin. This was derived by multiplying the theoretical value of σ_{sca} (D03) with the hydrogen column density toward Cyg X-2 that we measure.

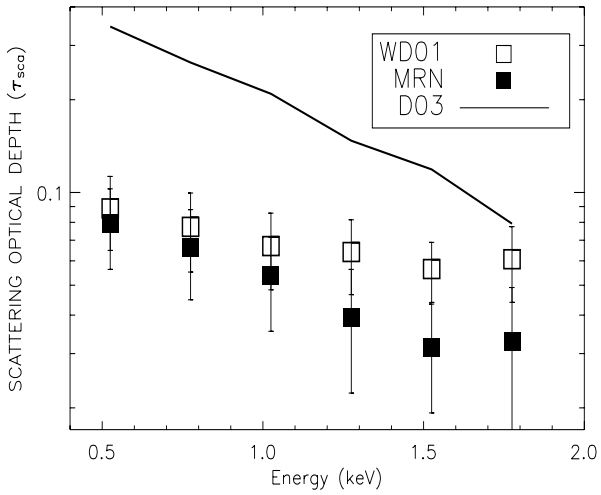

Fig. 10. The scattering optical depth as a function of energy, as measured from the SBP of Cyg X-2 halo for the MRN model (filled squares) and WD01 (empty squares). The data were collected in energy bins 0.25 keV wide. The solid line refers to the value of the total τ at the center of the bin, as predicted in D03.

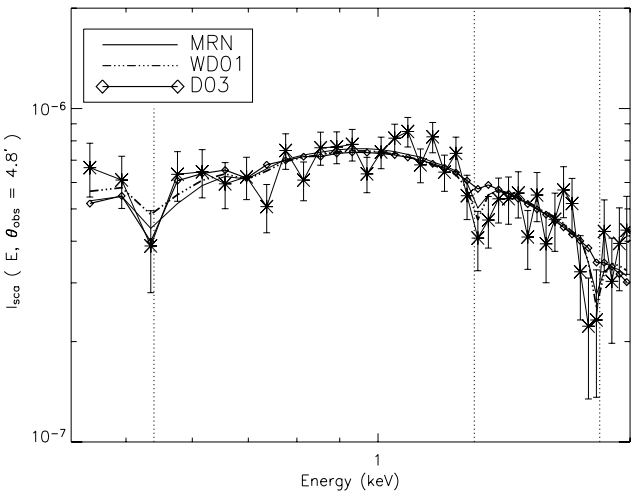

Fig. 11. EPIC-pn data of the Cyg X-2 halo, extracted at ~4.8′ from the source and PSF subtracted (asterisks), compared with the best-fit models: WD01 (dashed dotted line), MRN (solid line), and D03+WD01 model (diamonds). O-K, Mg-K, and Si-K edge energies are indicated by dotted lines.

5.2. Spectral modeling of the halo

In Fig. 11 we show the pure scattered radiation energy distribution (i.e. PSF subtracted), collected in a ring centered at 4.8′. The subtraction of the mirror scattering and of the central source contribution was described in Sect. 4. We avoid the data below 0.4 keV as the effective area calibration may still suffer from uncertainties in this range. At soft energies, the halo spectra collected in different annuli, shown in Fig. 7, do not vary dramatically (within statistical errors) among each other

after the PSF subtraction. Above 2 keV the differential scattering cross section does change dramatically as a function of the scattering angle (Fig. 1); however the contribution of the PSF wings is dominant at this energy and this change is unobservable in the present data. In principle, after the PSF subtraction, the modeling of the halo spectra, at each angular distance, would reveal the local properties of the dust grains. Indeed, inhomogeneity in the dust spatial distribution, size of the dust particles, and chemical composition would result in a spectral change. Unfortunately, these changes are tiny with respect to the instrumental uncertainties. The modeling here refers just to the ring around 4.8′, where the halo is brighter and thus the statistics are highest. The spectral features are still very well observable after the PSF subtraction. If artificially fitted with Gaussian profiles, the significance is 2.3σ, 3.2σ, and 4σ for O, Mg, and Si, respectively. Although the dust features of oxygen, magnesium and silicon are clearly detected in the scattered emission, still the statistics do not allow a unique interpretation of the data. In an attempt to give a quantitative picture of the observational evidence, we chose a model with only the dominant well-known compounds of the diffuse interstellar dust environment. We calculated the scattered intensity expected at the chosen angular distance, for the most common constituents of interstellar grains, i.e. graphite (carbon) and silicates. Silicates are found mostly in the form of $Mg_{2x}Fe_{2(1-x)}SiO_4$ and $MSiO_3$, where M is either Mg or Fe, thus we included olivine in the three different forms of $MgFeSiO_4$ (ρ = 3.8 g cm^{-3}), Fe_2SiO_4, (ρ = 4.39 g cm^{-3}) and Mg_2SiO_4 (ρ = 3.27 g cm^{-3}). Pyroxene are in the form of $MgSiO_3$ (ρ = 3.2 g cm^{-3}) and $FeSiO_3$ (ρ = 3.8 g cm^{-3}). For a given dust size distribution model (MRN or WD01), the relative contributions of the different grains materials are left as free parameters. Moreover, we considered also a model where only $MgFeSiO_4$ is taken as representative compound for silicates (D03). For this model, the dust size is distributed according to WD01, and in the scattering cross sections XAFS are included. The goodness of the fit was evaluated by minimizing χ^2.

The data are ignored below 0.4 keV, therefore we do not expect to put any constraint on the carbon component, whose main feature is at 0.28 keV. However, the carbon component is included in the fit since it may influence the shape of the continuum at energies above the carbon edge. Carbon contribution was allowed to vary between 20% and 30% of the total amount of dust (Whittet 2003), for all the models we tested. The data are modeled by a mixture of silicate and pyroxene. In Fig. 11 we display the three dust models tested. A mixture of silicate compounds (labeled MRN and WD01) seems to acceptably explain the data. C, O, Fe, Mg and Si alone account for 95% of the dust components. All elements except O account for 15–30% of the total amount of dust, in various forms (Whittet 2003). Here we assume that these elements describe 100% of the observed scattering. The linear combination of the compound contributions is shown in Fig. 12 for the MRN distribution. In the WD01 case, the combination of compounds is not significantly different from MRN (Fig. 11). The relative contribution to unity is Mg_2SiO_4 = 0.42, C = 0.26, $FeMgSiO_4$ = 0.054 and $FeSiO_3$ = 0.25. Fe_2SiO_4 and $MgSiO_3$ contribute a negligible fraction (<0.001). Counting the

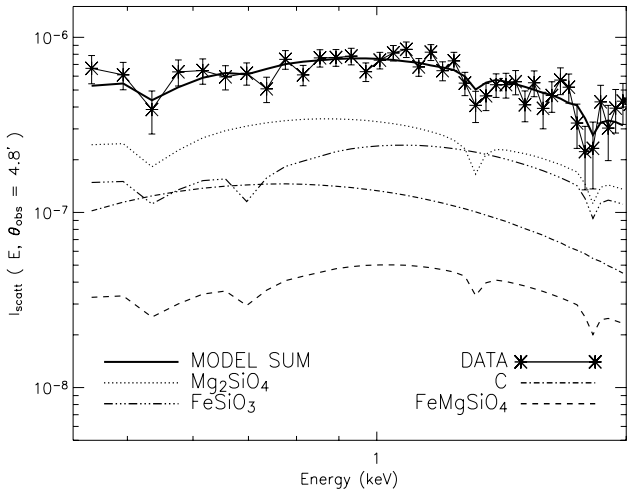

Fig. 12. Relative contributions to the best-fit model, using the MRN distribution. The data are the same as in Fig. 11.

contributions of the single elements, we obtain that roughly 42% of O, 26% of C, 11% and 13% of Si and Mg and 5% of Fe are needed to fit the data.

6. Discussion

6.1. The chemistry of dust grains

For the first time the signature of the elements locked in dust grains and responsible for the scattering of the X-rays has been detected. The best fit indicates a major contribution by olivine and pyroxene. We cannot exclude the presence of other compounds. A linear combination of scattered intensities for a given compound being the best fit, adding too many components would not necessarily be a true physical interpretation of the data. In principle, the depth of the spikes in the scattered spectrum tells us about the intrinsic properties of the dust grains. Magnesium and silicon are detected marginally in absorption (Fig. 3), while they are prominent features in the scattered spectrum, even in the raw data at the angles where the statistics is maximal (Fig. 7). Only a deeper observation will allow us to quantify this possible discrepancy by comparing the column densities for scattering and absorption derived for Mg and Si. As Fig. 3 shows, for an absorbing equivalent hydrogen column density of 2.2×10^{21} cm^{-2}, the iron L-shell at 0.706 keV is clearly measured. In the scattered spectrum iron is barely detectable. The best fit model (Fig. 12) requires a certain amount of Fe, although not precisely quantified, to be locked in silicates, with a Mg to Fe ratio of ∼5:(1.4–2.5). The depletion of Mg, as well as Si, depends on the density of the dust environment. Iron is found to be highly depleted (80–100%) from the intercloud medium to the densest environments. Thus, we can suppose that Mg is more abundant in silicates than Fe. In particular, a mixture of olivine and pyroxene with a ratio of 5:2 for Mg:Fe would account for the depletion of Mg and Si (Whittet 2003). In this framework, less than half of the available iron grains are locked in silicates and the rest in other forms. The best fit of the scattered halo at ∼4.8′, within errors, is in agreement with this simple prediction. If the lower limit is taken,

there would be more room for iron to be locked in other forms. Weingartner & Draine (1999) suggested, for instance, that up to 60% of Fe could be associated with graphite to form very small grains ($a \sim 10-15$ Å). An Mg:Fe ratio of 1:1, as prescribed by the D03 dust mixture, fails to explain the spectral energy distribution of the dust toward Cyg X-2. This again reinforces the idea that more compounds containing Mg and Si play a role in the scattering. As shown in Fig. 12, the data requires a major contribution of Mg_2SiO_4 rather than iron compounds like $FeSiO_3$. This dust mixture leads to a stronger contribution of Mg with respect to the D03 model.

This interpretation is influenced by the PSF subtraction, which can artificially enhance the depth of the Si feature (but not significantly for Mg which lies at 1.3 keV, where the halo is well above the the PSF) and the continuum around it (Sect. 4.2). Another unknown is the role of carbon. If the contribution of carbon between 0.4 and 2 keV varies substantially from the 20−30% of the total budget, then the contribution of silicate would need to be revisited. The quality of spectral data does not allow to notice a substantial discrepancy between the WD01 and MRN dust size distribution. As discussed below (Sect. 6.3), at the scattering angles we consider for the spectral analysis (around 4.8′), the bulk of the scattering is caused by grains with quite "standard" sizes and in this case the MRN and WD01 do not differ dramatically. However, with a deeper observation we would differentiate more between the two models at each scattering angle and this would influence the relative contribution to the scattering of the different compounds. We have seen that the modeling of Si suffers from the highest uncertainty in this analysis and we cannot draw any conclusion on the basis of this feature. However, the prominence of the Mg feature suggests a significant contribution of magnesium compounds. The oxygen region of the scattered spectrum is well interpreted by D03. This is because of the dielectric functions, which include XAFS near the edge energy (D03). When convolved with the spectral resolution of these data, such sub-structures are almost totally canceled: the difference in depth between the D03 and the Henke et al. (1993) dielectric functions are ∼1% for Mg and Si and ∼20% for iron. Oxygen is the only element where the discrepancy is noticeable (∼a factor two). Evaluating the contribution of the single elements, assuming that C, O, Fe, Mg and Si are causing the totality of the scattering, we find that oxygen can be completely explained in terms of silicate. This supports the idea that oxygen is preferably locked in these materials, leaving little room for other O compounds (e.g. OH, H_2O, Whittet et al. 2001), at least in the diffuse ISM. The features of the scattered halo, such as the ones shown in Fig. 11, were predicted by the scattering theory (e.g. Hayakawa 1970; Predehl & Klose 1996; D03). The dust physical parameters extracted from our modeling seems to bolster this interpretation. Another possibility for producing a complex halo spectrum would be an uneven absorption at an angular scale of arcminutes around the source. If, for example, the absorption toward the central source is few percent less than at the outer parts, the halo/source ratio will show extra absorption at soft energies, similar in shape to what we observe (Fig. 7). In this case, at the energy of the absorption edges, we would also expect broad and asymmetric residuals. However, we found the spectral shape of the halo to have circular symmetry around the central source and this is in conflict with a clumpy structure of the medium, and the features we observe in the scattered spectrum seem not to have an asymmetric, edge-like, shape. Moreover, there should be regions where, on the contrary, $N_{\rm H}$ is lower than toward the central source. In this case, the halo/source ratio should show an excess at soft energy and this was not observed. Although the assumption that in the diffuse ISM dust is homogeneously distributed is surely simplistic, in the case of Cyg X-2 we cannot prove that spatial variations of $N_{\rm H}$ on arcminute scales play a major role in the halo shape.

6.2. Oxygen in the ISM

The most prominent absorption features in the RGS band arise from oxygen transitions. The OI resonant line corresponding to the 1s–2p transition is clearly detected. Whether we can observe O in molecular form (Takei et al. 2003) is not obvious. The uncertainty is enhanced considering the lack of laboratory measurements for oxygen locked in compounds at these energies. The RGS resolution does not allow us to give a unique interpretation of the spectral region at energies higher than the oxygen edge. In terms of χ^2, the addition of one or possibly two more absorption edges or, alternatively, modeling the spectrum with three absorption lines (OI 1s − 3p, OII 1s − 2p, OIII, 1s − 2p), provides similar results. From the curve of growth analysis, Juett et al. (2004) calculate that the contribution of the ionized oxygen should be 10% of the neutral phase. The mildly ionized oxygen would then be produced by charge exchange with OI. However, in principle, absorption by oxygen in compounds is expected. In the present XMM-*Newton* observation, in addition to absorption, we could also study the scattering by ID and this allows us to state that oxygen locked in dust is actually present on the line of sight of Cyg X-2 (Fig. 11). The modeling of the halo spectrum shows that, to first order approximation, the oxygen feature is well explained if all the oxygen available in dust is locked in silicates. This translates into an oxygen to hydrogen ratio $O_{\rm dust}/H = 180$ ppm (Cardelli et al. 1996) in the line of sight to Cyg X-2. If the oxygen abundance O/H is taken to be 490 ppm (Wilms et al. 2000), then the depletion value for O, defined as the gas to total ISM ratio, is 0.63. With the total hydrogen column density derived from the RGS measurement ($N_{\rm H} \sim 2.2 \times 10^{21}$ cm^{-2}), we can then predict an absorption column density for oxygen locked in (silicate) dust. We obtain $N_{\rm abs}^{\rm O}$ for dust $\sim 3.85 \times 10^{17}$ cm^{-2}. In the Takei et al. (2003) model (Col. 1, Table 2), the edge attributed to oxygen in dust has an absorption optical depth of 0.27 ± 0.06 at 0.536 keV. Using the absorption cross section $\sigma_{\rm abs}^{\rm O} = 1.78 \times 10^{-19}$ cm^2, (D03, Li et al. 1995), the column density for this edge is $1.5^{+0.3}_{-0.4} \times 10^{17}$ cm^{-2}, which is too low compared to the theoretical value we obtained above. One possibility is that other absorption edges by oxygen in solid form are missing the detection. Indeed the energy and the structure of the edges slightly changes depending on which compound of oxygen and silicon is considered (e.g, Owens et al. 2002; Wong et al. 1995), and therefore some of them may be blurred and difficult to detect with the present resolution. This calculation

strongly depends on the adopted value of $\sigma^{\rm O}_{\rm abs}$. Here we considered the peak absorption cross section for oxygen locked in Mg_2SiO_4 (D03; Li et al. 1995), as determined by D03, with the underlying assumption that the oxygen edge profile is the same as the Si profile. However, small variations of $\sigma^{\rm O}_{\rm abs}$ lead to substantial variations of the value of $N_{\rm H}$. In fact, if the value $\sigma^{\rm O}_{\rm abs}$ is closer to that predicted for atomic oxygen ($\sigma = 4.8 \times 10^{-19}$, Verner & Yakovlev 1995; $\sigma = 3.85 \times 10^{-19}$, Henke et al. 1993), then the column density associated with the 0.536 keV edge is consistent with the value we obtained from the scattered radiation analysis. As a cautionary note, the effective area of EPIC-pn diminishes toward lower energy (60% less at 0.54 keV than at 1 keV) and the statistics of the oxygen feature may prevent us from obtaining a full description of the dust contribution to the total extinction. Moreover, the value for the total O/H ratio is not yet solidly established (Jensen et al. 2005, and references therein). Finally, the knowledge of the theoretical wavelengths of these dust absorption features is very fragmentary, making their interpretation difficult. Taking the $N^{\rm O}_{\rm abs}$ derived starting from the scattering analysis (and $\tau = N^{\rm O}_{\rm abs}\sigma^{\rm O}_{\rm abs} = 0.68$, if the D03 value is taken for σ) as an upper limit, absorption by oxygen in dust should be visible in absorption (edges and lines) using the RGS and instruments with even higher energy resolution (Takei et al. 2003).

6.3. The dust size distribution

In this XMM-*Newton* observation, the pile-up prevents us from studying the halo at angular radii smaller than ∼40″. This observational limit also hampers any detection of scattering either by large grains or standard grains located very close to the emitting source (Predehl & Klose 1996). Indeed these two conditions have the same effect of producing very narrow halo components in the profile. The data modeling of both the halo spatial profile and the halo spectral distribution show that both the MRN and WD01 dust size distribution can be applied despite the different amount of dust predicted for different scattering angles (Fig. 9). Grains with sizes >0.25 μm play a more important role in the WD01 model for radii $\lesssim$200″ at 1 keV. In the size range 0.001–0.25 μm, the MRN and WD01 models do not differ dramatically for $R_V = 3.1$ (see Fig. 2 of Weingartner & Draine 2001) and for the grain sizes roughly between 0.1–0.2 μm typically produce the bulk of the scattering halo at angular radii between 100″ and 1000″ (e.g., Mathis & Lee 1991; Draine & Tan 2003), which is the region that could be directly studied in the SBP of Cyg X-2. The contribution of small grains ($a \lesssim 0.05$) would be best investigated if we could access the region beyond 1000″, but unfortunately, in this observation the halo begins to fade, making the modeling challenging beyond ∼650″.

The value of the scattering optical depth derived from the SBP at 1 keV ($\tau_{\rm sca} = 0.054 \pm 0.018$) is larger, but consistent within the errors, with the value derived by the ROSAT halo ($\tau_{\rm sca} \sim 0.039$, PS95) obtained at ∼1.06 keV, if the MRN distribution is used. The PS95 modeling indeed started also from the MRN model, but leaving free some parameters in it, among which the maximum grain size and the slope of $n(a)$. Their best fit requires a maximum grain size of only 0.15 μm. This makes the halo model flatter and the derived value of $\tau_{\rm sca}$ lower than what we measure. The WD01 distribution predicts instead almost the double ($\tau_{\rm sca} = 0.067 \pm 0.018$) of the ROSAT result. This trend is visible at all energies (Fig. 10). This is mostly due to the increased scattering "power" by larger grains at smaller radii predicted by the WD01 (Fig. 9).

When the total scattering optical depth (for both MRN and WD01 case) as a function of energy is compared with a theoretical model (D03, Fig. 10), we see that it does not measure a substantial part of the scattered radiation. Indeed the model over-predicts the data at all energies apart from perhaps the last point. The distribution of $\tau_{\rm sca}$ flattens toward lower energies, while the model is significantly steeper. As noted in D03, the discrepancy was also found for other halo analysis (e.g., PS95, Smith et al. 2002; Woo et al. 1994). The Draine & Tan (2003) measurement instead has been found in agreement with the model (D03).

The value of $I_{\rm frac}$ (and thus of $\tau_{\rm sca}$), extracted at each energy, is model dependent and, moreover, can be substantially influenced by instrumental effects. For example, the scattering angle range accessible to this study (200″−600″) strongly privilege the observation of the scattering of 1−2 keV photons (e.g., Mathis & Lee 1991; D03), while the bulk of the emission for softer photons peaks at larger scattering angles. The estimated values for the total scattering optical depth, and in particular the ones related to the soft scattered photons are certainly lower limits. A significant fraction of the halo, in the form of fainter or narrower components, may be masked by the PSF wings (at small radii) or unaccessible because of the faint scattered emission with respect to the background (at larger radii).

6.4. The dust distribution along the line of sight

The distribution of dust along the line of sight could be studied through the SBP of the halo. The distribution of dust seems to be evenly distributed, at least for a fractional distance of the total path $x < 0.6$, corresponding to a linear distance between 4.3–6.7 kpc, (depending on the distance estimates for Cyg X-2; Orosz & Kuulkers 1999; Smale 1998). However, if the dust distribution is imposed to be uniform up to a fractional distance of 0.99 the fit worsens significantly suggesting that our line of sight passes through different dust clumps. A contribution from scattering events closer to the source is indeed likely to be present, but fainter or narrower halo components, as detected in other sources (e.g. Smith et al. 2002; Draine & Tan 2003; Costantini & Predehl 2005), cannot be investigated using XMM-*Newton* for radii < 12″ (and in any case not for Cyg X-2 because of the pile-up).

7. Conclusions

We have presented XMM-*Newton* results on the effect of scattering and absorption by ID along the line of sight to the bright X-ray binary Cyg X-2. This study led to the unprecedented detection of the elements in the ID responsible for the X-ray scattering: oxygen, magnesium and silicon. To first order, the modeling of the pure scattered radiation suggests a major

contribution of silicates in the form of olivine and pyroxene, in the energy range 0.4–2 keV. The best fit of the scattered spectrum shows that the ratio of Mg to Fe, locked in dust grains, is 5:(1.4:2.5). This is consistent with a picture in which Mg and Si are for the most part locked in silicates (Whittet 2003).

The contribution of carbon, a fundamental constituent of ID, could not be quantified as its most prominent feature (0.28 keV) lies below our selected EPIC-pn energy band. In the RGS spectrum, we studied the complexity around the oxygen edge, investigating the possibility of absorption by atomic and molecular oxygen, as suggested by Takei et al. (2002), in comparison with absorption by atomic neutral and ionized oxygen (Juett et al. 2004). The RGS resolution is not sufficient to support one interpretation over another, but the complementary information from the EPIC-pn analysis of the scattered spectrum allows us to detect oxygen locked in dust, preferably in the form of silicates. Starting from the scattered halo spectral modeling, we estimated that the absorption column density we expect by oxygen locked in silicates is indeed measurable using the RGS. The value of this column density seems too high compared to what measured for the absorption edge that Takei et al. (2003) interpret as arising from dust. However, instrumental/theoretical uncertainties makes this result not conclusive.

The study of the spectral energy distribution of the scattered radiation, performed in the halo region where the signal-to-noise ratio was best (around ∼4.8′), stressed the need of using an accurate theoretical approach to the data. The full Mie theory had to be used to model the data satisfactorily, especially below 2 keV where the chemistry of the halo can now be studied. This approach was already applied to ROSAT data (Smith & Dwek 1998; Draine & Tan 2003). With XMM-*Newton* we could extend this analysis, performing spatially resolved spectroscopy of the halo that could not be interpreted unless the Mie differential scattering cross section was used.

The modeling of the SBP shows that the dust is uniformly distributed along the line of sight at least for a fractional distance of the total path $x < 0.6$, corresponding to a linear distance between 4.3–6.7 kpc, depending on the source distance estimates. However, a uniform dust distribution along the complete path toward Cyg X-2 is not required by the data, hinting to a clumped structure of the dust for $x > 0.6$. Within the instrumental uncertainties, the data are acceptably fit by both a MRN and a WD01 dust size distribution. The inferred scattering optical depth is approximately 0.054 and 0.067 at 1 keV for the MRN and WD01 distribution, respectively. We extended the modeling of the SBP of the halo to the 0.4–2 keV band. The derived values of the total $\tau_{\rm sca}$ as a function of energy are systematically lower than that predicted by theory (D03), pointing out that some halo components may be easily missed due to instrumental effects.

Acknowledgements. The authors thank the referee, Prof. B.T. Draine, for his valuable comments which improved the quality of the paper. This project was developed for the most part during the stay of E.C. at the Max-Planck-Institut für extraterrestrische Physik. E.C. wishes to thank also K.C. Steenbrugge and F. Verbunt for carefully reading this manuscript. The XMM-*Newton* project is supported by the Bundesministerium für Bildung und Forschung/Deutsches Zentrum für Luft- und Raumfahrt (BMBF/DLR), the Max-Planck-Gesellschaft and the Heidenhain-Stiftung.

References

Bradt, H. V. D., & McClintock, J. E. 1983, ARA&A, 21, 13
Cardelli, J. A., Meyer, D. M., Jura, M., & Savage, B. D. 1996, ApJ, 467, 334
Cartledge, S. I. B., Lauroesch, J. T., Meyer, D. M., & Sofia, U. J. 2004, ApJ, 613, 1037
Costantini, E., & Predehl, P. 2005, in preparation
Dame, T. M., Hartmann, D., & Thaddeus, P. 2001, ApJ, 547, 792
den Herder, J. W., Brinkman, A. C., Kahn, S. M., et al. 2001, A&A, 365, L7
de Vries, C. P., den Herder, J. W., Kaastra, J. S., et al. 2003, A&A, 404, 959
Dickey, J. M., & Lockman, F. J. 1990, ARA&A, 28, 215
Di Salvo, T., Farinelli, R., Burderi, L., et al. 2002, A&A, 386, 535
Draine, B. T. 2003, ApJ, 598, 1026 (D03)
Draine, B. T., & Tan, J. C. 2003, ApJ, 594, 347
Freyberg, M. J., The XMM-Newton EPIC-pn camera: Spectral and Temporal properties of the internal background (XMM-Newton Calibration Report, June 2003)
Gallagher, D., Cash, W., & Green, J. 1995, ApJ, 439, 976
Ghizzardi, S. 2002, In Flight Calibration of the PSF for the PN Camera, XMM-Newton Calibration Report, EPIC-MCT-TN-012, `http://xmm.vilspa.esa.es/docs/documents/CAL-TN-0029-1.0.ps.gz`
Gorczyca, T. W., & McLaughlin, B. M. 2000, Journal of Physics B Atomic Molecular Physics, 33, L859
Hayakawa, S. 1970, Prog. Theor. Phys., 43, 1224
Henke, B. L., Gullikson, E. M., & Davis, J. C. 1993, Atomic Data and Nuclear Data Tables, 54, 181
Jensen, A. G., Rachford, B. L., & Snow, T. P. 2005, ApJ, 619, 891
Juett, A. M., Schulz, N. S., & Chakrabarty, D. 2004, ApJ, 612, 308
Li, D., Bancroft, G. M., Fleet, M. E., & Feng. X. H. 1995, Phys. Chem. Minerals, 22, 115
Landgraf, M., Baggaley, W. J., Grün, E., Krüger, H., & Linkert, G. 2000, J. Geophys. Res., 105, 10343
Lee, J. C., Reynolds, C. S., Remillard, R., et al. 2002, ApJ, 567, 1102
Mathis, J. S., & Whiffen, G. 1989, ApJ, 341, 808
Mathis, J. S., & Lee, C.-W. 1991, ApJ, 376, 490
Mathis, J. S., Rumpl, W., & Nordsieck, K. H. 1977, ApJ, 217, 425 (MRN)
Mathis, J. S., Cohen, D., Finley, J. P., & Krautter, J. 1995, ApJ, 449, 320
Mauche, C. W., & Gorenstein, P. 1986, ApJ, 302, 371
McLaughlin, B. M., & Kirby, K. P. 1998, Journal of Physics B Atomic Molecular Physics, 31, 4991
Mie, G. 1908, Ann. Phys. Lpz., 25, 377
Mitsuda, K., Inoue, H., Koyama, K., et al. 1984, PASJ, 36, 741
Overbeck, J. W. 1965, ApJ, 141, 864
Orosz, J. A., & Kuulkers, E. 1999, MNRAS, 305, 132
Owens, A., Fraser, G. W., & Gurman, S. J. 2002, Radiation Physics and Chemistry, 65, 109
Predehl, P., & Klose, S. 1996, A&A, 306, 283
Predehl, P., & Schmitt, J. H. M. M. 1995, A&A, 293, 889 (PS95)
Read, A. M., & Ponman, T. J. 2003, A&A, 409, 395
Smale, A. P. 1998, ApJ, 498, L141

Smith, R. K., & Dwek, E. 1998, ApJ, 503, 831
Smith, R. K., Edgar, R. J., & Shafer, R. A. 2002, ApJ, 581, 562
Snow, T. P., & Witt, A. N. 1995, Science, 270, 1455
Strüder, L., Briel, U., Dennerl, K., et al. 2001, A&A, 365, L18
Takei, Y., Fujimoto, R., Mitsuda, K., & Onaka .T. 2003, ApJ, 581, 307
Titarchuk, L. 1994, ApJ, 434, 570
Turner, M. J. L., Abbey, A., Arnaud, M., et al. 2001, A&A, 365, L27
van de Hulst, H. C. 1957, Light Scattering by Small Particles (New York: John Wiley & Sons)
Verner, D. A., & Yakovlev, D. G. 1995, A&AS, 109, 125
Weingartner, J. C., & Draine, B. T. 1999, ApJ, 517, 292
Weingartner, J. C., & Draine, B. T. 2001, ApJ, 548, 296 (WD01)
Whittet, D. C. B., Pendleton, Y. J., Gibb, E. L., et al. 2001, ApJ, 550, 793
Whittet, D. C. B. 2003, Dust in the galactic environment, 2nd ed., ed. C.B. Whittet (Bristol: Institute of Physics (IOP) Publishing), Ser. Astron. Astrophys.
Wilms, J., Allen, A., & McCray, R. 2000 ApJ, 542, 914
Wiscombe, W. J. 1980, Applied Optics, 19, 1505
Witt, A. N., Smith, R. K., & Dwek, E. 2001, ApJ, 550, L201
Wong, J., et al. 1995, Physica B Condensed Matter, 208, 220
Woo, J. W., Clark, G. W., Day, C. S. R., Nagase, F., & Takeshima, T. 1994, ApJ, 436, L5